communications earth & environment

A Nature Portfolio journal

Article

https://doi.org/10.1038/s43247-026-03368-4

Satellite retrieved soil surface dynamics reduce the extent and frequency of sediment flux with implications for early warning systems

Check for updates

Zhuoli Zhou[1,2], Adrian Chappell[2]✉, Chunlai Zhang[1]✉ & Hongquan Song[3]

Wind-driven sediment transport causes severe land degradation, soil carbon loss, and atmospheric dust emissions. Society relies on sediment transport models for climate-dust interactions, early warnings of sand and dust storms, reduced air quality and transport hazards. However, models have long assumed fixed sediment initiation threshold and unlimited sediment supply. Here we present comprehensive data from satellite retrievals and new wind tunnel measurements, which matches previous field studies and shows dynamic thresholds feedback to reduce sediment supply. We reveal that the magnitude and frequency of sediment transport events are misrepresented by current models. Globally, dynamic thresholds decrease unrealistic fluxes by 45% in mainly vegetated and rough-surfaced areas which reduces wind erosion-effected areas by 69% (~ 40% of the Earth's land surface). Large scale models used in society's applications must include dynamic soil surface conditions to adequately represent dust emission and operate early warning systems for sand and dust-related hazards and sustainable land use/management.

Sand and dust storms (SDS) increase soil erosion, leading to soil carbon loss and reduced soil fertility (e.g., wind-driven SOC losses of ~75 Tg C yr^{-1} reported for China)[1,2], deterioration of air quality and human health impacts[3], degraded vegetation cover and modified ecosystems[4], and substantial impacts on food security and the environment[5]. Nearly four decades ago, physically based aeolian entrainment threshold (u_{*ts}) modelling was developed to quantify drag and lift forces of the soil surface wind friction velocity (u_{s*}) overcoming gravitational and inter-particle cohesive forces[6–8]. The modelling described u_{*ts} assuming soil surfaces were loose, erodible and with segregated particle diameters and an endless sediment supply (Fig. 1). This enabled modelling to predict u_{*ts} using particle size data fixed over large homogeneous spatial soil texture classes and static over time. The entrainment of these size fractions is considered separately by sediment transport equations which underpin dust emission schemes[9–12]. The modelling has remained unchanged for nearly 40 years despite being unrealistic and well-known to neglect commonly occurring, highly heterogeneous, soil surface conditions[13,14] (e.g., loose, sealed, crusted and rocky). These conditions change over space and time due to weathering processes and sediment fluxes (Fig. 1), changing soil properties like moisture[15–17], roughness[18,19] and crusting[20,21]. Consequently, the known feedback between dynamic u_{*ts} and soil surface wind friction velocity (u_{s*})[22,23] is excluded in SDS modelling.

Empirical (e.g., Revised Wind Erosion eQuation; RWEQ) modelling is being increasingly used to make regional and global estimates of sediment transport to quantify changes in patterns and trends, to attribute cause, and support mitigation measures and policy-making[24–27]. However, empirical modelling has the same threshold weaknesses and endless sediment supply assumptions as classic physically based transport modelling. These simplifying model assumptions are important because the magnitude of modelled sediment transport (and dust emission) depends on the frequency that u_{s*} exceeds u_{*ts}[28]. The impact for modelling of changing sediment supply is expected to be profound for dust emission, reducing by an order of magnitude for a single event, and suggesting that global dust emission estimates may be substantially over-estimated[29]. The correct magnitude of u_{*ts} and how it changes over time is therefore critical for sediment supply and the modelling accuracy and precision of sediment transport (and dust emission) magnitude and frequency[30].

---

[1]State Key Laboratory of Earth Surface Processes and Disaster Risk Reduction, MOE Engineering Research Center of Desertification and Blown-sand Control, Faculty of Geographical Science, Beijing Normal University, Beijing, China. [2]School of Earth and Environmental Sciences, Cardiff University, Cardiff, UK. [3]State Key Laboratory of Spatial Datum, College of Remote Sensing and Geoinformatics Engineering, Faculty of Geographical Science and Engineering, Henan University, Zhengzhou, China. ✉e-mail: ChappellA2@cardiff.ac.uk; clzhang@bnu.edu.cn

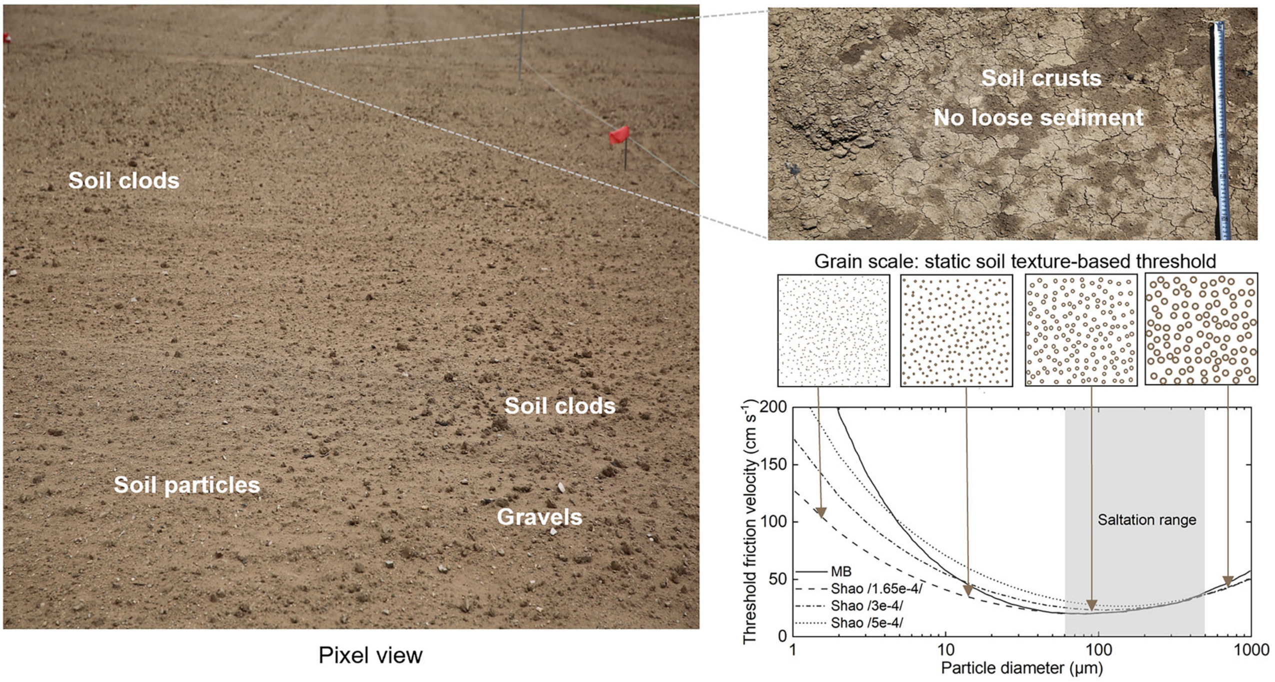

Fig. 1 | The classical entrainment threshold in sand and dust storm models. The threshold of a point is assumed to be represented by the (depth-bulked) soil texture which excludes the changing condition of the soil surface. The naturally heterogeneous mixture of aggregate sizes comprising the soil texture over area, is assumed segregated into several relatively homogeneous particle diameter size fractions. Model curves shown are based on Darmenova et al.[65] (their Fig. 3). MB and Shao denote the thresholds from Marticorena and Bergametti[9] and Shao and Lu[7] (including parameters representing varying cohesive forces), respectively.

It is well-established over the last 60 years that observed and numerically modelled changes in albedo represent dynamic soil surface processes associated with roughness, including the sheltering of the soil surface by vegetation cover, the formation of crusts or soil clods with large surface roughness, and particle size and cracking of the soil surface[31–35]. These processes contribute to temporal feedback that modify surface roughness over time, which in turn affects the entrainment thresholds. Chappell and Webb[36] developed a calibration between normalised shadow and wind tunnel aerodynamics to calculate areal u_{s*} from albedo, which scales linearly with area[37,38]. This method addresses dust emission model resolution limitations[39] and the mismatch between point-scale parameterisations and areal wind fields used in large-scale modelling[12]. Here, we retrieve soil surface conditions over space and time and establish an albedo-based dynamic sediment entrainment threshold to accurately represent changing magnitude and frequency[28]. The retrieval is validated against field threshold measurements and verified against field transport measurements, which are geographically limited, and then applied globally across different land cover types.

Results

Novel dynamic entrainment areal thresholds (dEARTH)

We established a new calibration between laboratory measurements of soil surface wide-angle albedo, narrow-angle reflectance and wind tunnel measured entrainment threshold of soil particles and aggregates diameters. The widely used theoretical expression for the entrainment threshold of loose, dry spherical particles is a function of particle diameter $u_{*ts}(d)$[7] (Methods Eq. (1)). In this study, d represents a single particle diameter, within a distribution of particle diameter sizes associated with the soil texture of the soil (0–5 cm). The D denotes the equivalent soil surface aggregate diameter retrieved from the soil surface roughness (hereafter: equivalent roughness aggregate diameter). We compared our new threshold measured in wind tunnel experiments with the theoretical threshold curve of Shao and Lu[7] to evaluate our measurements (Fig. 2). Figure 2a illustrates the relation with long-standing theory between the dimensionless threshold wind friction velocity (A; Methods Eq. (2)) and the particle Reynolds number (Re_{*t}; Methods Eq. (3)) of our measurements, plotted with some existing studies[40]. On fine particle surfaces, interparticle cohesive forces caused entrainment threshold to increase rapidly. For our loose, dry quartz and sandy soils, there was a strong positive correlation and regression relation of the areal soil surface normalised shadow ($AS\omega_{ns}$; Fig. 2 also Methods Section "New albedo-based dynamic entrainment areal thresholds (dEARTH)", Eq. (11)) with aggregate diameter D and Reynolds number Re_{*t} (Fig. 2b). These new results indicate that $AS\omega_{ns}$ adequately represents the smooth surface roughness of size-segregated equivalent roughness aggregate diameters. We plotted thresholds of different particle diameters for the cleaned quartz material and separate sandy soil and compared them with the theoretical curve of Shao and Lu[7] (Fig. 2c) used in classic SDS modelling. Our measured thresholds were entirely consistent with that established theoretical curve. With the strong relation between $AS\omega_{ns}$ and D, and following the same form of the Shao and Lu[7] threshold model, we replaced the equivalent roughness aggregate diameter D with $AS\omega_{ns}$ to obtain the entrainment threshold $u_{*ts}(\omega)$ (Methods Section "New albedo-based dynamic entrainment areal thresholds (dEARTH)"; Eq. (13)). The small uncertainty represented by the square root of the mean squared difference ($\mathrm{RMSE} = 0.075\ \mathrm{m\,s^{-1}}$) confirms the high quality performance and enables retrieval of dynamically changing threshold over space and time using albedo data from ground, airborne or satellite platforms (Fig. 2d).

To independently evaluate the performance of the new dynamic entrainment thresholds model under in situ surface conditions, we collated PI-SWERL data from the literature (see Supplement S1). We focused on four publications[41–44] with a total of 130 measurements from a wide variety of surface types with thresholds from $0.2\ \mathrm{m\,s^{-1}}$ to $1\ \mathrm{m\,s^{-1}}$ (Fig. 3a, b). We identified the coordinates and dates of the PI-SWERL measurements and calculated the texture-based threshold following the classic approach and retrieved the new dynamic thresholds (Methods Section "Classic sediment entrainment threshold" & "New albedo-based dynamic entrainment areal thresholds (dEARTH)"). The texture-based threshold is generally smaller than the PI-SWERL measurements (Fig. 3a; $R^2 = 0.45$). The new dynamic thresholds correlate similarly well with the PI-SWERL measurements (Fig. 3b; $R^2 = 0.48$) demonstrating confidence in the new model. At sites

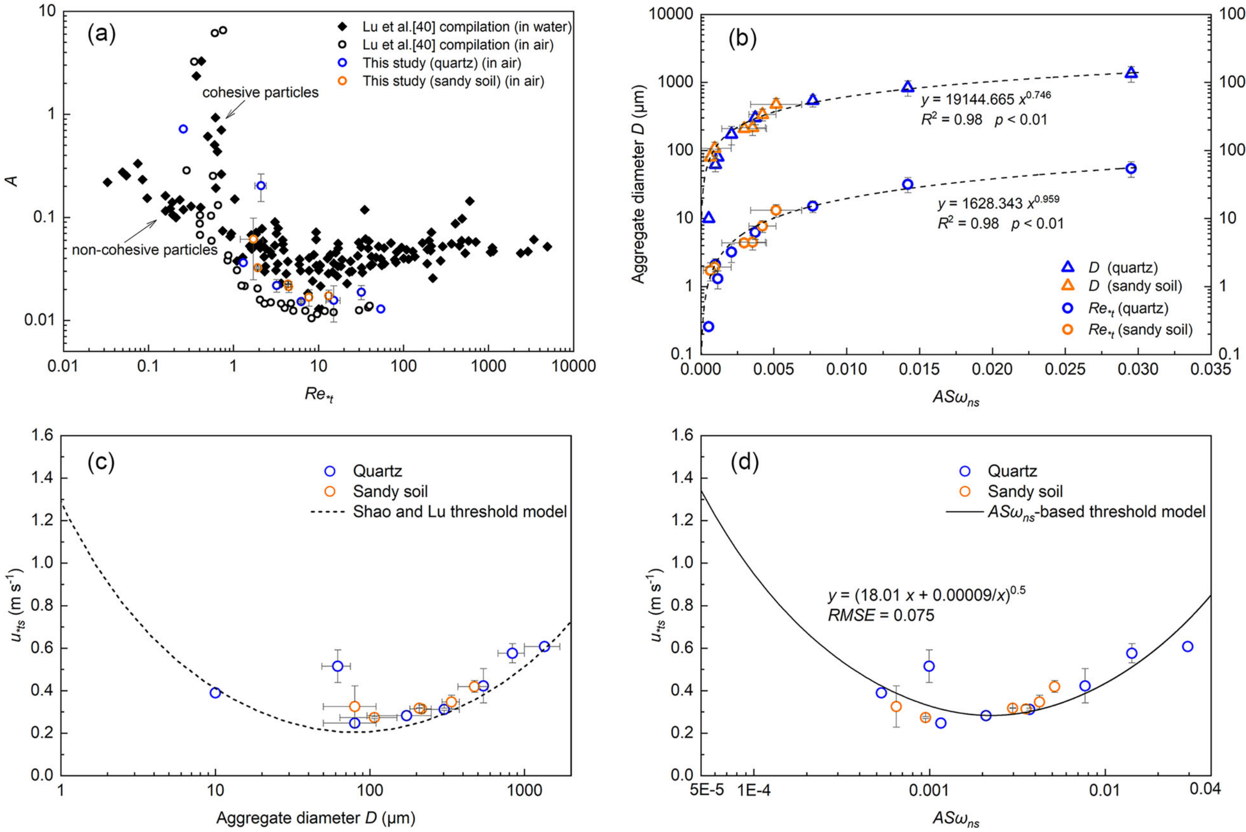

Fig. 2 | Calibration of sediment entrainment thresholds. The dimensionless threshold wind friction velocity A plotted against the particle Reynolds number Re_{*t} modified from Lu et al.[40] (their Fig. 1) (**a**). The $AS\omega_{ns}$ had a strong correlation when plotted against the measured average equivalent roughness aggregate diameter D (μm) of the sieved size fraction and the particle Reynolds number Re_{*t} (**b**). Sediment entrainment threshold u_{*ts} measured in wind tunnel experiments plotted against aggregate diameter D (μm) and the dashed line represents the threshold model of Shao and Lu[7] (**c**). The measured threshold u_{*ts} plotted against $AS\omega_{ns}$ and the solid line is an empirical threshold model based on the $AS\omega_{ns}$ calibration (**d**). Error bars represent variability derived from repeated measurements.

prone to sediment transport (thresholds 0.2–0.6 m s^{-1}), thresholds are highly consistent. However, sites less prone to sediment transport (>0.6 m s^{-1}) e.g., stone-paved surfaces reported by Cui et al.[41], PI-SWERL measurements were larger than the new thresholds. Attributed differences between PI-SWERL measurements and the new model are explained in the Supplement (S1).

To evaluate the overall performance of the modelling, we plotted the sediment transport using the classic texture-based approach $Q_{CT}(d)$ and that from the new dynamic thresholds $Q_{AT}(\omega)$, against sediment transport from our wind tunnel measurements and from recent field transport measurements (Fig. 3c, d; Supplement S7, 8). The results showed a similarly strong relation in both cases demonstrating confidence in our new dynamic threshold and overall modelling. A magnitude adjustment ($c = 2.87$) was required indicating that measurements are more than twice the magnitude of the modelled sediment transport (Supplement S4).

Model performance was also evaluated by comparing the modelled sediment transport over time to the field-measured transport[45] at the monthly scale (Fig. 3e). The $Q_{AT}(\omega)$ was smaller than $Q_{CT}(d)$ using the RMSE = 328.15 g m^{-1} d^{-1} and the mean absolute difference (MAE = 155.56 g m^{-1} d^{-1}) between the model and measurements. These statistics indicated that $Q_{AT}(\omega)$ provided a more accurate representation of the temporal variations in observed sediment transport fluxes. The modelled cumulative frequency distribution quantiles are plotted against the quantiles of the transport measurement distribution (q-q plot) to show (dis)similarity in the distributions (Fig. 3f). The simulated values from the $Q_{AT}(\omega)$ model are distributed closer to the 1:1 line than $Q_{CT}(d)$ indicating better agreement with the measured distribution. In contrast, the $Q_{CT}(d)$ model exhibits larger overall bias and overestimates large sediment transport fluxes.

Impact of dynamic entrainment areal thresholds (dEARTH) for sand and dust storm modelling

Wind erosion is a dynamic process, and the heterogeneous soil surface conditions that influence wind erosion can change daily, seasonally, and annually[13,46]. The new threshold showed spatial variability across most regions prone to sand and dust storms (Supplement S2, Supplementary Fig. S1). The soil surface changes as sediment transport occurs, producing feedback between the soil surface wind friction velocity (u_{s*}) and the entrainment threshold (u_{*ts})[22,23]. To illustrate our novel dynamic entrainment threshold $u_{*ts}(\omega)$ and its utility for SDS modelling, we selected four different types of sites (Fig. 4; also Supplement S3, Supplementary Fig. S2) that are prone to sediment transport. We used the Google Earth Engine which included the MODIS albedo archive to retrieve all the necessary information.

We plotted over time the new dynamic threshold $u_{*ts}(\omega)$ and the classic static texture-based threshold $u_{*ts}(d)$. We compared both with the soil surface wind friction velocity in the classic model $u_{s*} = u_* R$, where u_* is the above canopy wind friction velocity (Fig. 4; left column green line) and the drag partition $R = 0.91$, following Zender et al.[47]. We also included the albedo-based u_{s*} (Fig. 4; left column orange line). We calculated the magnitude and frequency of sediment transport (Fig. 4; right column) following Wolman and Miller[28]. In the classic model, u_* provides the magnitude (m). In North Africa and the Middle East where there is little-to-no (vegetation) roughness canopy, $u_* \approx u_{s*}$ (P1; Fig. 4). However, where a roughness canopy causes a partition in drag, $u_* > u_{s*}$ with implications for sediment transport[48] as evident at the other sites (P2–P4; Fig. 4). The thresholds at all sites (Fig. 4; left column) changed relatively smoothly and independently of the relatively erratic fluctuations of u_{s*}. The $u_{*ts}(\omega)$ varies more, and has larger values, than the $u_{*ts}(d)$ (Fig. 4; left column; solid blue and dashed blue

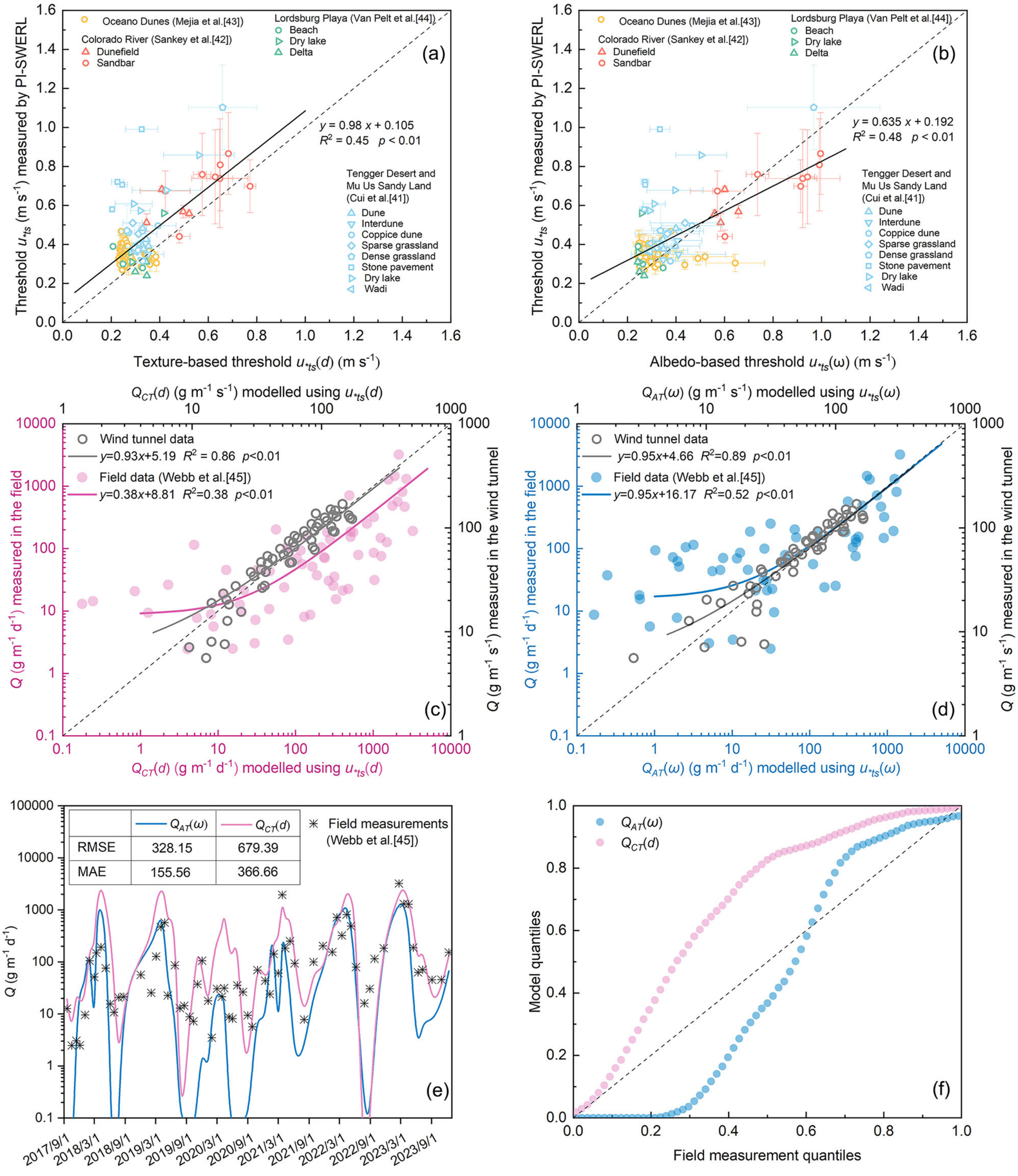

Fig. 3 | Validation of entrainment thresholds and sediment transport. Texture-based threshold $u_{*ts}(d)$(**a**) and albedo-based new threshold $u_{*ts}(\omega)$ (**b**) plotted against measured entrainment threshold from PI-SWERL studies (see Supplement S1). Error bars are included only where the original studies have made many measurements in one pixel. In addition, PI-SWERL represents thresholds under the specific soil moisture conditions present at the time of measurement. While Cui et al.[41] and Sankey et al.[42] provided soil moisture data for their sampling points, Mejia et al.[43] and Van Pelt et al.[44] did not. For these last two studies, we used modelled (0–5 cm) soil moisture data from ERA5-Land and adjusted the new albedo-based thresholds using the soil moisture function of Fécan et al.[15] following the standard practice in sediment transport and dust emission modelling. Verification of sediment transport modelled using texture-based threshold $u_{*ts}(d)$ (**c**) and albedo-based new threshold $u_{*ts}(\omega)$ (**d**) against wind tunnel measured sediment transport from this study (see Supplement S7) and field transport measurements[45] (see Supplement S). These data are adjusted to the 1:1 line using the dimensionless fitting coefficient ($c = 2.87$; Supplement S4). Model performance was evaluated by comparing over time the modelled sediment transport using the classic texture-based approach $Q_{CT}(d)$ and that from the new dynamic thresholds $Q_{AT}(\omega)$ (see Supplement S4) with field transport measurements (**e**). The modelled cumulative frequency distribution quantiles are plotted against the quantiles of the transport measurement distribution (q-q plot) to show (dis)similarity in the distributions (**f**).

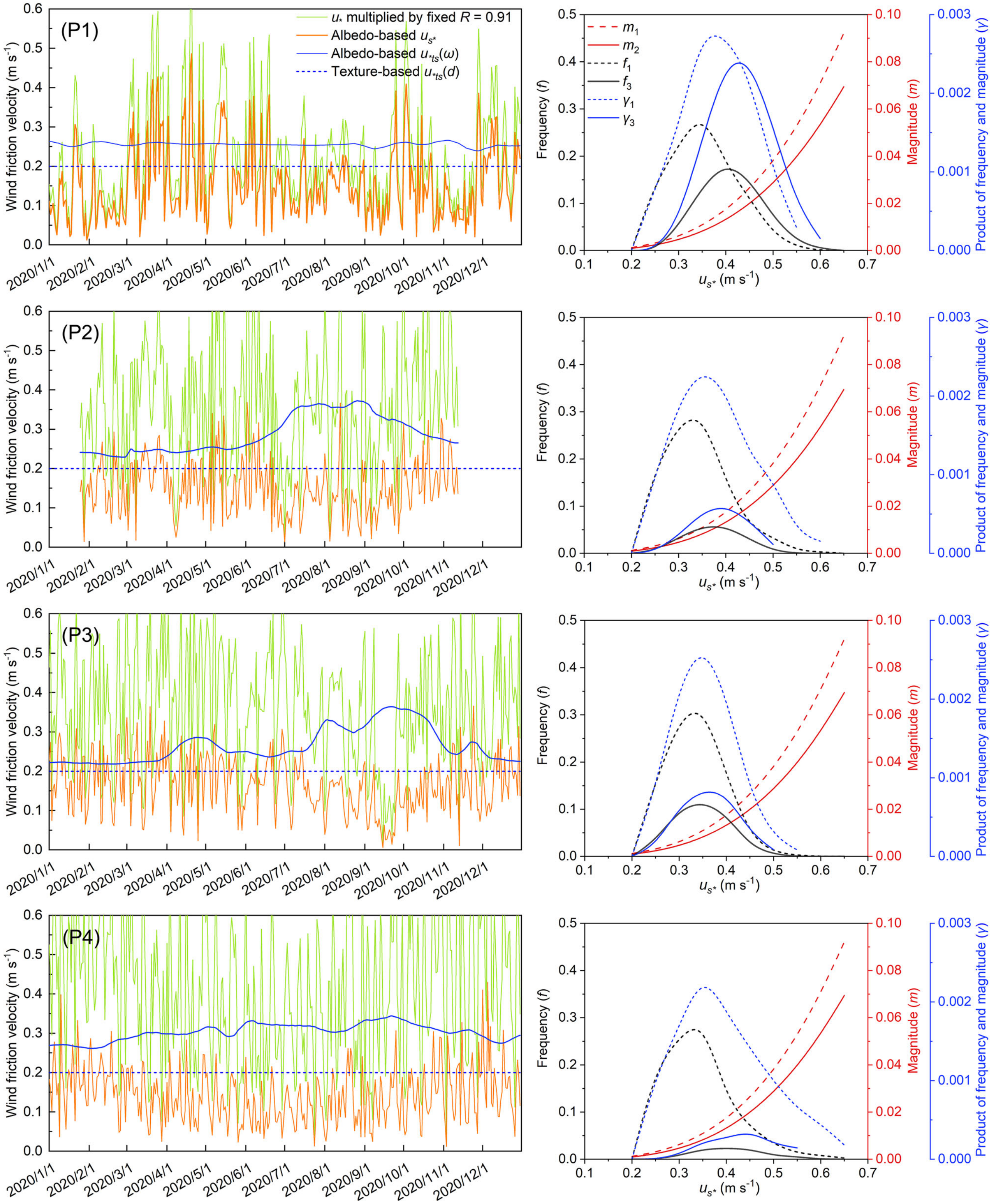

Fig. 4 | Effects of dynamic entrainment thresholds on sediment transport magnitude and frequency. Daily time series (for year 2020) of MODIS normalised albedo-based soil surface wind friction velocity (u_{s*}), classic $u_{s*} = u_* R$ where $R = 0.91$ (in the classic model, R was used for threshold adjustment only), normalised albedo-based threshold $u_{*ts}(\omega)$ and classic texture-based threshold $u_{*ts}(d) = 0.2$ m s^{-1} at four sites (Left column). The sites were P1: desert in Algeria, North Africa (lon: 8.97°; lat: 30.97°); P2: grassland in the Inner Mongolia Autonomous Region, China (snow caused missing data in January and December; lon: 115.17°; lat: 44.87°); P3: cropland in Texas, USA (lon: -101.54°; lat: 32.29°); P4: scrubland in New South Wales, Australia (lon: 142.60°, lat: −29.81°). The right column shows the magnitude (m; kg m^{-1} s^{-1}) and frequency (f) multiplied (γ; kg m^{-1} s^{-1}; following Wolman and Miller[28]) to produce sediment transport at the four sites. The magnitude curves are (see Supplement S4) classic $m_1 = c\frac{\rho_a}{g}u_*^3$ (kg m^{-1} s^{-1}) and albedo-based $m_2 = c\frac{\rho_a}{g}u_{s*}^3$ (kg m^{-1} s^{-1}); the frequency curves are $f_1 = u_* R > u_{*ts}(d)$, and $f_3 = u_{s*} > u_{*ts}(\omega)$; the product curves are $\gamma_1 = m_1 \times f_1$ (kg m^{-1} s^{-1}) and $\gamma_3 = m_2 \times f_3$ (kg m^{-1} s^{-1}). Note thresholds here exclude adjustments due to the soil moisture function $H(w)$ to ensure that the illustrations include only the influence of the dynamic threshold.

lines, respectively). Consequently, there are many fewer occurrences of modelled sediment transport using the $u_{*ts}(\omega)$. In contrast, the excessive magnitude (u_*^3)[48] and small, fixed threshold of the classic SDS modelling (Fig. 4; left column green and blue dashed lines) produces very large frequency of occurrence and which produces large sediment transport (Fig. 4; right column). Consequently, the classic modelled transport at the three sites with vegetation roughness canopy (P2–P4) is greater than that of the North African desert site (P1), where the canopy is absent. By showing the differences in the magnitude and frequency combinations described by fixed spatial and static temporal thresholds versus dynamic spatial and temporal thresholds, we demonstrate how the use of incorrect (non-dynamic) thresholds can lead to extreme and unrealistic sediment transport predictions.

For the year 2024, we present the modelled sediment transport flux using the texture-based threshold (Fig. 5a, b) and the new dynamic entrainment thresholds (Fig. 5c). Consistent with the details for the individual sites (Fig. 4), the classic texture-based threshold produces sediment transport over 78 million km^2, which considerably exceeds (175% of 44.5 million km^2; Supplement S4, Supplementary Fig. S3) the global drylands area. Its transport occurs in the well-known dust source regions but also across vast, densely vegetated swathes where transport is unlikely (e.g., South America; Fig. 5a). The albedo-based texture entrainment threshold has considerably reduced the transport area caused solely by its dynamic drag partition (Fig. 5b). The new *dEARTH* model reveals that the global area effected by sediment transport (24 million km^2) is 69% smaller than the area of the classic model and 54% of drylands (Fig. 5c; Supplement S4, Supplementary Fig. S3; Supplementary Table S5). Its global average frequency of occurrence over time (304 hours y^{-1}) is smaller than the classic model (442 hours y^{-1}; Fig. 5g; Supplement S4, Supplementary Fig. S4). Sediment transport at those pixels (10.6 Mg ha^{-1} y^{-1}) is also smaller than the classic texture-based model (26.3 Mg ha^{-1} y^{-1}; Fig. 5d–f; Supplement S4, Supplementary Fig. S5). Sediment transport frequency varies seasonally, and there is considerable seasonal difference between the classic model and the other models (outside North Africa and the Middle East) mostly in Australia (Fig. 5g). The largest transport occurs in North Africa and the Middle East during March-August.

The new *dEARTH* model estimates global transport mass (102.2 Pg y^{-1}) 45% smaller than the classic model (186.6 Pg y^{-1}; Fig. 5h). Sediment transport is reduced in all regions except North Africa ($R = 0.91$ is fixed in classic SDS modelling so that dust emission matches measured dust optical depth; Fig. 5a). Overall, the new *dEARTH* model demonstrates that accuracy and precision in sediment transport (underpinning dust emission modelling) depends on adequately representing the magnitude and frequency of occurrence.

To extend the visualisation, we have provided an animation of daily u_{s*} exceeding the new $u_{*ts}(\omega)$ (see Supplementary Movie 1) during the year 2022. In the animation, the relatively slowly changing greyscale (white to black) background is the $u_{*ts}(\omega)$ and also illustrates changing snow cover over Earth. The rapidly changing colours (yellow, pink and red) are where and when the $u_{s*} > u_{*ts}(\omega)$ and therefore represent (small, medium and large) sediment transport. Dynamic change in soil surface conditions and changing sediment supply can be seen when the light-coloured pixels (small threshold) become dark coloured (large threshold), typically after transport occurs (flashes of yellow colour).

Discussion

In the Earth system, mineral particles do not typically exist dispersed in the soil as assumed by classic modelling. Rather, the soil surface comprises aggregates or crusts due to the physical, chemical and biological cohesive forces between the particles[14]. Biocrusts cover about 12% of the Earth's land surface and reduce global atmospheric dust emissions by about 60%[21]. Similarly, soil surface conditions are affected through processes like aggregation, crust formation, and clod development[14]. These surface roughness characteristics strongly impact the wind friction velocity exerted on aggregates at the soil surface[13]. The new dynamic entrainment areal threshold (*dEARTH*) model describes sparse, discontinuous sediment transport over time and space (Figs. 4 and 5; Supplementary Fig. S3) consistent with observed occurrences from remote sensing e.g., dust emission point sources[30,49,50].

The new *dEARTH* model reveals that the global area effected by sediment transport (24 million km^2) is 69% smaller than the area of the classic model (78 million km^2). That difference in area (54 million km^2), no longer modelled as affected by sediment transport, is around 40% of the Earth's land surface. The new model estimates global transport mass of 102.2 Pg y^{-1}, which is 45% smaller than the classic model (186.6 Pg y^{-1}) and reduces sediment transport regionally relative to the classic model (with the explained exception of North Africa). Notably, the region around the Bodélé Depression has consistently one of the largest occurrences of sediment transport across all modelling (Fig. 5a, c). The threshold weaknesses and assumed endless sediment supply is evidently an adequate approximation in the Bodélé region where sediment supply is long-lasting, caused by quartz aggregate abrasion of diatomite fragments[51,52]. However, apparent model consistency in the Horn of Africa is, in the absence of evidence for strong dust emission[53], very likely caused by erroneously large wind speeds[30], which are beyond the scope of this study.

The probability of occurrence (frequency) of sediment transport varies markedly across different regions (Supplement S4, Supplementary Table S3). Barren land has the greatest occurrence (except in the Americas) followed by minor grassland and shrubland contributions and negligible cropland contributions (except in Central Asia) potentially due to sustainable land management practices and increased awareness of maintaining crop cover or at least a rough surface during fallow periods. The global average frequency of occurrence over time (304 hours y^{-1}; 13 days per year) suggests the satellite observed dust emission point source (DPS) frequency (~7 days per year)[54] are under-estimates as expected[30]. That discrepancy is very likely due to the satellite DPS data missing small events and those that occur only close to the land surface[30].

Empirical modelling (RWEQ) has the same threshold weaknesses and endless sediment supply as classic transport modelling. Despite using fractional canopy cover, empirical modelling over-estimates sediment transport area by six times (e.g., 130 million km^2)[26]. Regional empirical erosion estimates for China (36 Mg ha^{-1} y^{-1})[55], southern Africa (up to 170 Mg ha^{-1} y^{-1})[24] and the African continent (166 Mg ha^{-1} y^{-1})[25] are all over-estimated. Consequently, the empirical global total annual average is over-estimated by a factor of 3 to 4 (312–359 Pg y^{-1})[26,27]. Estimates of empirical global average wind erosion per unit area, are also approximately 3 to 4 times larger (37–52 Mg ha^{-1} y^{-1})[26,27] than the new *dEARTH* model.

Our new *dEARTH* model demonstrates the importance of accurate and precise representation of magnitude and frequency of occurrence[28]. Evidently, classic modelling has not adequately represented the spatio-temporal variation in entrainment threshold by assuming heterogeneous soil surface conditions are decomposed into loose, erodible segregated particle diameters. Classic and empirical modelling omit the dynamic soil surface conditions, which limit sediment supply and cause over-estimated sediment flux, with profound implications for dust modelling[29]. Similarly, our findings have considerable implications for modelling in this the UN decade (2025–2034) to combat sand and dust storms and particularly the development of dust emission modelling[30]. Importantly, the new *dEARTH* model will very likely enable reconciliation between spatio-temporal dust emission model estimates and atmospheric dust measurements[30].

Dynamic entrainment areal thresholds (dEARTH) can be monitored from ground-based or satellite remote sensing data, or with prognostic albedo in large-scale modelling[12]. We can therefore represent across measurement, monitoring and modelling scales for the first time, the previously omitted impacts of dynamic entrainment thresholds on sediment transport and dust emission modelling. Similarly, these new insights to soil erodibility can now be considered alongside the more commonly considered erosivity explanations for changing regional dust[46,56,57] providing new opportunities for more realistic interpretations of environmental change.

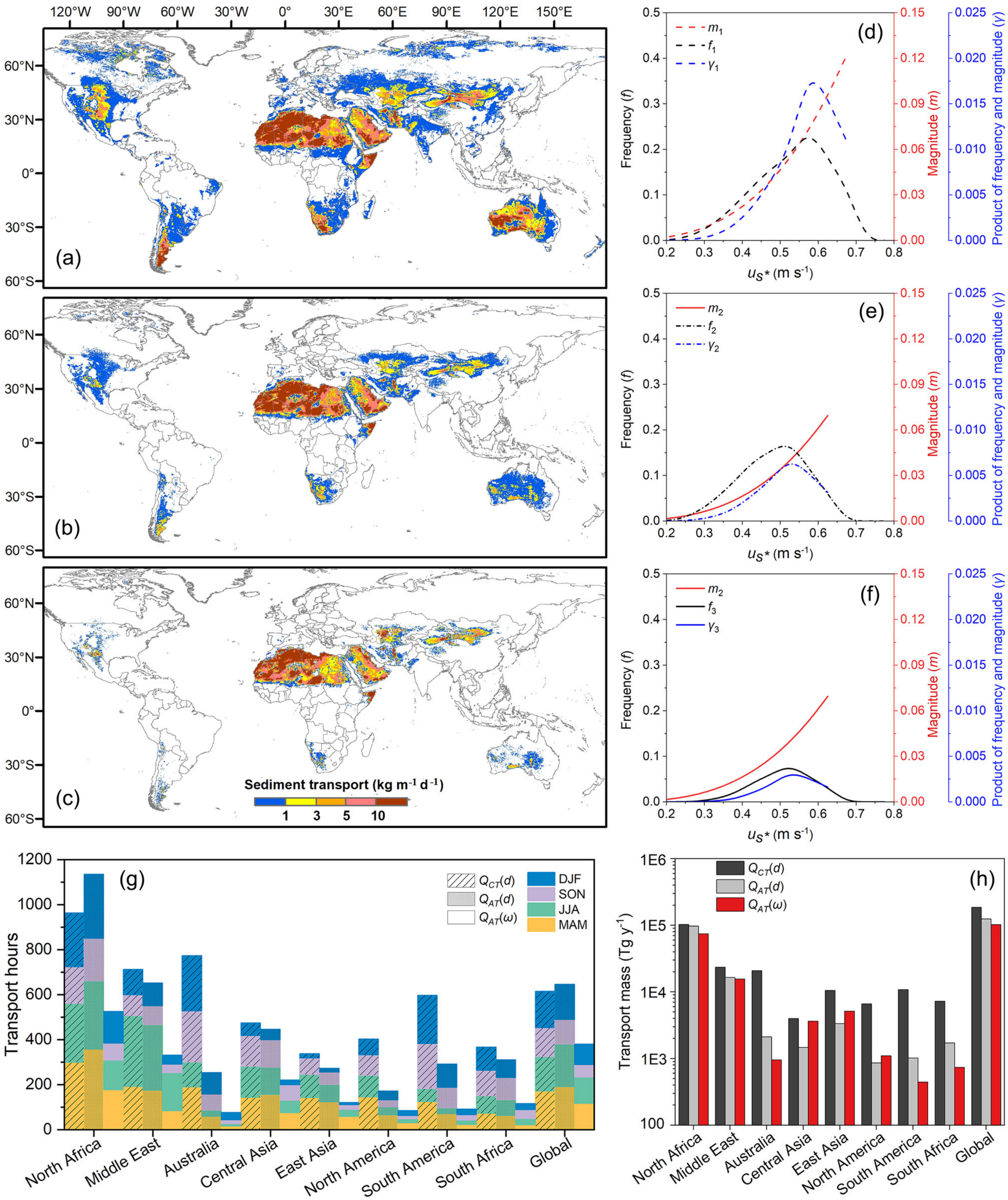

Fig. 5 | Global sediment transport estimated using different modelling schemes. Sediment transport during 2024 using the same wind speed and soil moisture data (see Supplement S4; Supplementary Table S1) for the classic model with a texture-based threshold $Q_{CT}(d)$ (**a**), the albedo-based model using a texture-based threshold $Q_{AT}(d)$ (**b**), and the albedo-based model using a new dynamic entrainment threshold ($Q_{AT}(\omega)$; **c**). We used random sampling of 1000 pixels across the eroding area, stratified by regions/land cover types, to obtain the magnitude (m; kg m^{-1} s^{-1}) and frequency (f) multiplied to produce (γ; kg m^{-1} s^{-1}; Wolman and Miller[28]) the global sediment transport for $Q_{CT}(d)$ (**d**), $Q_{AT}(d)$ (**e**), and $Q_{AT}(\omega)$ (**f**). The curves are calculated in the same way as in Fig. 4 (see Fig. 4 caption; here $f_2 = u_{s*} > u_{*ts}(d)$ and $\gamma_2 = m_2 \times f_2$ (kg m^{-1} s^{-1})). The seasonal (December-February, DJF; March-May, MAM; June-August, JJA; September-November, SON) variation contributing sediment transport across the main source regions (**g**). The total transport mass for the year 2024 (**h**), is calculated for the three models (Supplement S4, Supplementary Table S2). The sediment transport rate (kg m^{-1} s^{-1}) derived from each model was first converted into a gross erosion modulus using 500 m pixels scaled by the contributing proportion R (kg m^{-2} s^{-1}). Here, R was applied as a scaling factor to represent the fraction of the soil surface wind friction velocity that effectively contributes to wind erosion within the pixel (see Supplement S4; Supplementary Eq. (S6); sediment delivery ratio used in water erosion). The total transport mass (Tg y^{-1}) for each region was obtained by summing the erosion values across all contributing pixels (each representing a pixel area as the square of the pixel).

This study has several limitations that require additional work. First, threshold measurements for fine particles remain technically challenging, introducing greater uncertainty in threshold values for very fine particles[40]. Second, our calculation of normalised shadowed vegetation ($V\omega_{ns}$) used to derive $AS\omega_{ns}$, assumes a constant. Although we showed that constant did not influence the modelling, data on the variability of that parameter value may improve the estimates. Finally, our model validation is constrained by the data we used. The sediment transport observations were collected at the monthly scale and cannot directly validate high-frequency erosion events. Those datasets mainly originate from North American wind erosion regions. Measurements from other major source areas, such as Central and East Asia, and North Africa are not expected to be much different. However, their larger magnitude values would extend the validation. Access to broader spatial coverage and finer temporal-resolution observations would further strengthen the impact of dynamic entrainment threshold on sediment transport and dust emission modelling.

Methods

Classic sediment entrainment threshold

The widely used theoretical expression for the entrainment threshold of dry, loose and spherical particles is a function of particle diameter (d)[7]:

$$u_{*ts}(d) = \sqrt{A_N\left(\frac{\rho_p g d}{\rho_a} + \frac{\Gamma}{\rho_a d}\right)}, \tag{1}$$

where $A_N = 0.0123$, a dimensionless scaling coefficient theoretically determined by the particle friction Reynolds number, although empirical data suggests that A_N remains nearly constant[58]. The values for particle density $\rho_p = 2650\ \mathrm{kg\ m^{-3}}$, air density $\rho_a = 1.23\ \mathrm{kg\ m^{-3}}$, $g = 9.81\ \mathrm{m\ s^{-2}}$ (acceleration due to gravity), and $\Gamma = 0.000165\ \mathrm{kg\ s^{-2}}$ (a parameter representing particle cohesive forces) are also specified. We compared the threshold measured in wind tunnel experiments with the theoretical threshold curves of Shao and Lu[7] to evaluate the measurements.

A universal relationship between the dimensionless threshold wind friction velocity (A) and the particle Reynolds number (Re_{*t}) has been demonstrated in long-standing threshold theory[40]:

$$A = \frac{\rho_a {u_{*ts}}^2}{(\rho_p - \rho_a) g d} \tag{2}$$

$$\mathrm{Re}_{*t} = \frac{u_{*ts}\, d}{\nu} \tag{3}$$

where ν is the kinematic viscosity of the fluid. Lu et al.[40] demonstrated the relationship between A and Re_{*t} from wind tunnel measurements and compared it with values in the literature. The value of d (Eq. (2)) is determined by fixed soil texture data in applications.

New albedo-based dynamic entrainment areal thresholds (dEARTH)

To produce a dynamic albedo-based areal sediment entrainment threshold we assume that the particle diameter (and Reynolds number) characterises the smooth (without roughness elements) soil surface roughness of an area and is a function of areal soil shelter. We can then develop a new threshold to replace the particle diameter (d; μm) in the Shao and Lu[7] model to calculate u_{*ts} using albedo which is area-weighted and integrated across aggregate sizes and more specifically, represents the soil surface condition over area (pixel). Our study uses (i) an artificial quartz sediment of the same particle density cleaned of aggregates and therefore with separate particle sizes and (ii) a naturally aggregated aeolian sediment with mixed particle densities obtained from the field, sieved into different aggregate sizes (Supplementary S5). These two types of material enabled the experiment to investigate the difference in threshold between disaggregated and aggregated material and therefore represent a wide range of soil. We measured the albedo and reflectance of each particle and aggregate size (Supplementary S6) and determined the entrainment threshold for each surface using wind tunnel experiments (Supplementary S7).

Chappell and Webb[36] developed the following equations to calibrate direct beam (black-sky) albedo using ray-casting with wind tunnel aerodynamic measurements[59] as the ratio of wind friction velocities above roughness canopies (u_*) and soil surfaces (u_{s*}) to the wind speed (U) at freestream (U_f):

$$\frac{u_*}{U_f} = 0.0497\left(1 - \exp\frac{-{\omega_{ns}}^{1.326}}{0.0027}\right) + 0.038 \tag{4}$$

$$\frac{u_{s*}}{U_f} = 0.0311\left(\exp\frac{-{\omega_{ns}}^{1.131}}{0.016}\right) + 0.007 \tag{5}$$

The drag partition (R) is the wind friction velocity on the bare soil surface (u_{s*}) to the wind friction velocity above roughness canopies (u_*), which can therefore be readily calculated as $R = u_{s*}/u_*$ using Eqs. (4) and (5).

The albedo was converted to shadow and normalised (ω_{ns}) for retrieval from MODIS data (MODIS/006/MCD43A1) using the data catalogue of the Google Earth Engine. To ensure the MODIS-based shadow aligns with the calibration relationships derived from Marshall's[59] wind tunnel data, the data was scaled using the following equation:

$$\omega_{ns} = \frac{(a-b)(\omega_n(\theta) - \omega_n(\theta)_{\max})}{(\omega_n(\theta)_{\min} - \omega_n(\theta)_{\max})} + b \tag{6}$$

where $a = 0.0001$, $b = 0.1$, $\omega_{n.\min} = 0$, and $\omega_{n.\max} = 35$. Following advice from the MODIS team (pers. comm. Prof. Crystal Schaaf) and demonstration by Chappell et al.[60], we used the MODIS isotropic parameter f_{iso} to remove spectral effects due to soil properties such as the moisture content, mineral composition, and soil organic carbon content to calculate the normalised land surface shadow of a pixel (ω_n). Theoretically and in practice, the retrieved structural information does not vary with waveband[31,33,34,60], and we calculated ω_n using MODIS Band 1 (620–670 nm):

$$\omega_n = \frac{1 - \omega_{dir}(\theta, \nu)}{f_{iso}(\nu)} = \frac{1 - \omega_{dir}(0^\circ)}{f_{iso}} \tag{7}$$

where $\omega_{dir}(\theta, \nu)$ is the albedo at a given solar zenith angle ($\theta = 0°$) and given waveband (ν), and f_{iso} is an isotropically weighted parameter from the MODIS BRDF model that represents the spectral contribution from the surface.

For data measured in the wind tunnel experiments, we calculated ω_{ns} using the same Eq. (6) but with calibration parameters changed to $\omega_{n.\min} = 2.50$ and $\omega_{n.\max} = 12$, respectively. Since the artificially disaggregated quartz material was partially transparent (translucent), we corrected the normalised shadow of quartz to be consistent with the normalised shadow of the naturally aggregated opaque sandy soil. We obtained the relation between the soil ω_n and particle diameter for sandy soil. The ω_n values were then calculated based on the particle diameter of the quartz sediment.

For consistency with the established areal albedo-based model (Eqs. (4) and (5) above) we require a new parameterisation for areal albedo-based sediment entrainment threshold. Although the normalised shadow of the land surface pixel (vegetation and soil) is available (ω_{ns}) we require shadow of the soil surface (without vegetation) which is not currently available over large areas, suitable for modelling. The key to implementing our new parameterization is analogous to decomposing the contributions of pixel reflectance[61]. The common challenge is that pixel decomposition requires both the reflectance $\rho(0^\circ, \lambda)$ and its areal contribution to the total pixel (A_T) of several components, and the solution is similarly under-constrained.

Instead of considering the waveband dependent reflectance of each contribution in the pixel, we consider the normalised shadow which is waveband independent, and the pixel decomposition becomes well constrained, as follows. For a given area or pixel and at nadir view zenith angle (θ=0°), $\omega_{ns}(\theta)$ is partitioned between the illuminated vegetation $V\omega_i(\theta)$, illuminated soil surface $S\omega_i(\theta)$, normalised shadowed vegetation $V\omega_{ns}(\theta)$ and the normalised shadowed soil surface $S\omega_{ns}(\theta)$:

$$\omega_{ns}A_T = V\omega_i A_{iv} + S\omega_i A_{is} + V\omega_{ns}A_{nv} + S\omega_{ns}A_{ns}, \tag{8}$$

and requires their respective contributing areas (A_T, A_{iv}, A_{is}, A_{nv}, A_{ns}). With respect to their shadow contribution, the reflectance of illuminated vegetation $V\omega_i$ and illuminated soil surface $S\omega_i$ are so small that they may be assumed negligible and set to 0, consistent with previous approaches (e.g., Wanner et al.[62]). However, their areal contribution continues to influence the contributing areas. If the areal contributions are assumed to sum to $A_T = 1$ and rearranged:

$$\omega_{ns} = V\omega_{ns}A_{nv} + S\omega_{ns}A_{ns}, \tag{9}$$

we have values of ω_{ns} for each pixel and $V\omega_{ns}$ is the normalised shadow of vegetation, without any contribution from the underlying soil. The remaining unknown quantities are the areal contributions of the normalised shadow of vegetation (A_{nv}) and that of the soil surface (A_{ns}). We assume that these quantities are equivalent to the R drag partition (Eqs. (4) and (5)) with the pixel-scale shadow providing an approximation of the associated sheltering effect, and set $A_{nv} = 1 - R$ and $A_{ns} = R$ to produce a linear relation between ω_{ns} and $S\omega_{ns}$:

$$\omega_{ns} = V\omega_{ns}(1 - R) + S\omega_{ns}R, \tag{10}$$

In the absence of any other information at this stage, we assume that $V\omega_{ns} \approx 0.006$ is a constant and show the model's (Eq. (10)) small sensitivity to this assumption when entrainment threshold $u_{*ts}(\omega) < 0.6\ \mathrm{m\ s^{-1}}$ (typical of the maxima from field measurements associated with sediment transport) by plotting ω_{ns} against the entrainment threshold for different values of $V\omega_{ns}$ (Supplementary S9, Supplementary Fig. (S10)).

When $R = 0$, the soil in the pixel is entirely sheltered from the wind's momentum by the large scale, typically vegetation roughness, $\omega_{ns} = V\omega_{ns}$. When $R = 1$, the pixel is devoid of vegetation, $\omega_{ns} = S\omega_{ns}$ and sheltered only be the small scale, typically soil roughness. When $0 < R < 1$, ω_{ns} comprises both large-scale vegetation shelter and small-scale soil shelter. The soil contribution $S\omega_{ns}$ is the rearrangement and called $AS\omega_{ns}$:

$$AS\omega_{ns} = S\omega_{ns}.R = \omega_{ns} - V\omega_{ns}(1 - R) \tag{11}$$

Notably, the drag partition (R) depends on the exposed (unsheltered) contribution from soil and vegetation and is related to the albedo-derived components, deduced using the preceding equations, or could be measured separately:

$$R = \frac{u_{s*}}{u_*} = \frac{(\omega_{ns} - V\omega_{ns})}{(S\omega_{ns} - V\omega_{ns})}. \tag{12}$$

Since $0 \le R \le 1$, when $\omega_{ns} > V\omega_{ns}$ and $S\omega_{ns} > V\omega_{ns}$, $S\omega_{ns} > \omega_{ns}$. Similarly, when $\omega_{ns} < V\omega_{ns}$, $S\omega_{ns} < V\omega_{ns}$ and $S\omega_{ns} < \omega_{ns}$. For wind-tunnel simulations of soil samples, $R \rightarrow 1$.

To replace the fixed soil particle size (d) with readily retrievable area-weighted soil shadow $AS\omega_{ns}$ =($S\omega_{ns}.R$) and obtain the dynamic u_{*ts}, we used the same functional form as proposed by Shao and Lu[7]:

$$u_{*ts}(AS\omega_{ns}) = \sqrt{a\,AS\omega_{ns} + \frac{b}{AS\omega_{ns}}}, \tag{13}$$

where $a = 18.01$ ($\mathrm{m^2\ s^{-2}}$) and $b = 0.00009$ ($\mathrm{m^2\ s^{-2}}$) are fitting constants determined from our wind tunnel measurements (Fig. 2d; RMSE = 0.075) and d is replaced with $AS\omega_{ns}$ (Eq. (11)).

We already established consistency between: (i) numerical simulations of direct beam, black sky albedo (directional hemispherical reflectance; DHR) normalised by reflectance; (ii) retrievals of MODIS black sky albedo normalised by f_{iso}; (iii) field measurements of direct beam albedo using pyranometers divided by narrow angle, broadband reflectance by plotting their relations with each other and the theoretical curves (Zhou et al.[38]; Figs. 4 and 5). This demonstrates that all these approaches are consistent and are DHR. Furthermore, we showed that calibrated pyranometer albedo-based $S\omega_{ns}$, $AS\omega_{ns}$, and ω_{ns} from the field were consistent with MODIS black sky albedo-based estimates (Supplementary S9, Supplementary Fig. S11).

Reporting summary

Further information on research design is available in the Nature Portfolio Reporting Summary linked to this article.

Data availability

The data supporting the figures of this study are available via Zenodo (https://doi.org/10.5281/zenodo.18565743)[63]. Data used for global-scale modelling were accessed via Google Earth Engine, with details provided in Supplementary Table S1.

Code availability

Custom scripts used for modelling in the Google Earth Engine (GEE) are available via Zenodo (https://doi.org/10.5281/zenodo.18599174)[64].

Received: 23 September 2025; Accepted: 25 February 2026;
Published online: 14 March 2026

References

1. Yan, H., Wang, S., Wang, C., Zhang, G. & Patel, N. Losses of soil organic carbon under wind erosion in China. *Glob. Change Biol.* **11**, 828–840 (2005).
2. Lal, R. Accelerated Soil erosion as a source of atmospheric CO_2. *Soil Tillage Res.* **188**, 35–40 (2019).
3. Tian, M., Gao, J., Zhang, L., Zhang, H., Feng, C. & Jia, X. Effects of dust emissions from wind erosion of soil on ambient air quality. *Atmos. Pollut. Res.* **12**, 101108 (2021).
4. Duniway, M. C., Pfennigwerth, A. A., Fick, S. E., Nauman, T. W., Belnap, J. & Barger, N. N. Wind erosion and dust from US drylands: a review of causes, consequences, and solutions in a changing world. *Ecosphere* **10**, e02650 (2019).
5. Middleton, N. Impacts of sand and dust storms on food production. *Environ. Res. Food Syst.* **1**, 022003 (2024).
6. Greeley, R., and Iversen, J. D. (1985) *Wind as a geological process on Earth, Mars, Venus and Titan* (Cambridge Univ. Press, 1985).
7. Shao, Y. & Lu, H. A simple expression for wind erosion threshold friction velocity. *J. Geophys. Res. Atmos.* **105**, 22437–22443 (2000).
8. Pähtz, T., Clark, A. H., Valyrakis, M. & Durán, O. The physics of sediment transport initiation, cessation, and entrainment across aeolian and fluvial environments. *Rev. Geophys.* **58**, e2019RG000679 (2020).
9. Marticorena, B. & Bergametti, G. Modeling the atmospheric dust cycle: 1. Design of a soil-derived dust emission scheme. *J. Geophys. Res. Atmos.* **100**, 16415–16430 (1995).
10. Shao, Y., Raupach, M. R. & Leys, J. F. A model for predicting aeolian sand drift and dust entrainment on scales from paddock to region. *Aust. J. Soil Res.* **34**, 309–342 (1996).
11. Kok, J. F., Storelvmo, T., Karydis, V. A., Adebiyi, A. A., Mahowald, N. M., Evan, A. T., He, C. & Leung, D. M. Mineral dust aerosol impacts on global climate and climate change. *Nat. Rev. Earth Environ.* **4**, 71–86 (2023).

12. Chappell, A. et al. Elucidating hidden and enduring weaknesses in dust emission modelling. *J. Geophys. Res. Atmos.* **128**, e2023JD038584 (2023).
13. Zobeck, T. M. Soil properties affecting wind erosion. *J. Soil Water Conserv.* **46**, 112–118 (1991).
14. Webb, N. P. & Strong, C. L. Soil erodibility dynamics and its representation for wind erosion and dust emission models. *Aeolian Res.* **3**, 165–172 (2011).
15. Fécan, F., Marticorena, B. & Bergametti, G. Parameterization of the increase of the aeolian erosion threshold wind friction velocity due to soil moisture for arid and semi-arid areas. *Ann. Geophys.* **17**, 149–157 (1999).
16. Dong, Z., Mu, Q. & Liu, X. Defining the threshold wind velocity for moistened sediments. *J. Geophys. Res. Solid Earth* **112**, B08202 (2007).
17. Sharratt, B. S., Vaddella, V. K. & Feng, G. Threshold friction velocity influenced by wetness of soils within the Columbia Plateau. *Aeolian Res.* **9**, 175–182 (2013).
18. King, J., Nickling, W. G. & Gillies, J. A. Representation of vegetation and other nonerodible elements in aeolian shear stress partitioning models for predicting transport threshold. *J. Geophys. Res. Earth Surf.* **110**, F04015 (2005).
19. Buyantogtokh, B. et al. Effect of stones on the sand saltation threshold during natural sand and dust storms in a stony desert in Tsogt-Ovoo in the Gobi Desert, Mongolia. *J. Arid Land* **13**, 653–673 (2021).
20. O'Brien, P. & Neuman, C. M. A wind tunnel study of particle kinematics during crust rupture and erosion. *Geomorphology* **174**, 149–160 (2012).
21. Rodriguez-Caballero, E. et al. Global cycling and climate effects of aeolian dust controlled by biological soil crusts. *Nat. Geosci.* **15**, 458–463 (2022).
22. Stout, J. E. Simultaneous observations of the critical aeolian threshold of two surfaces. *Geomorphology* **85**, 3–6 (2007).
23. Stout, J. E. & Arimoto, R. Threshold wind velocities for sand movement in the Mescalero Sands of southeastern New Mexico. *J. Arid Environ.* **74**, 1456–1460 (2010).
24. Zhao, C., Zhang, H., Wang, M., Jiang, H., Peng, J. & Wang, Y. Impacts of climate change on wind erosion in Southern Africa between 1991 and 2015. *Land Degrad. Dev.* **32**, 2169–2182 (2021).
25. Zhang, H., Peng, J. & Zhao, C. Wind speed and vegetation coverage in turn dominated wind erosion change with increasing aridity in Africa. *Earths Future* **12**, e2024EF004468 (2024).
26. Chu, Z. et al. & Wang, X. Spatiotemporal distribution of global wind erosion over the past four decades. *Environ. Res. Lett.* **19**, 114019 (2024).
27. Sun, R. et al. Global wind erosion reduction driven by changing climate and land use. *Earths Future* **12**, e2024EF004930 (2024).
28. Wolman, M. G. & Miller, J. P. Magnitude and frequency of forces in geomorphic processes. *J. Geol.* **68**, 54–74 (1960).
29. Shao, Y. et al. Source limitation could have major implications to dust emission estimates. *Geophys. Res. Lett.* **52**, e2024GL112562 (2025).
30. Chappell, A. et al. Satellites reveal Earth's seasonally shifting dust emission sources. *Sci. Total Environ.* **883**, 163452 (2023).
31. Hapke, B. W. A theoretical photometric function for the lunar surface. *J. Geophys. Res.* **68**, 4571–4586 (1963).
32. Cierniewski, J. A model for soil surface roughness influence on the spectral response of bare soils in the visible and near-infrared range. *Remote Sens. Environ.* **23**, 97–115 (1987).
33. Pinty, B., Verstraete, M. M. & Dickinson, R. E. A physical model for predicting bidirectional reflectances over bare soil. *Remote Sens. Environ.* **27**, 273–288 (1989).
34. Jacquemoud, S., Baret, F. & Hanocq, J. F. Modeling spectral and bidirectional soil reflectance. *Remote Sens. Environ.* **41**, 123–132 (1992).
35. Chappell, A., Zobeck, T. M. & Brunner, G. Using bi-directional soil spectral reflectance to model soil surface changes induced by rainfall and wind-tunnel abrasion. *Remote Sens. Environ.* **102**, 328–343 (2006).
36. Chappell, A. & Webb, N. P. Using albedo to reform wind erosion modelling, mapping and monitoring. *Aeolian Res.* **23**, 63–78 (2016).
37. Ziegler, N. P., Webb, N. P., Chappell, A. & LeGrand, S. L. Scale invariance of albedo-based wind friction velocity. *J. Geophys. Res. Atmos.* **125**, e2019JD031978 (2020).
38. Zhou, Z. et al. Using field measurements across land cover types to evaluate albedo-based wind friction velocity and estimate sediment transport. *J. Geophys. Res. Atmos.* **129**, e2023JD040313 (2024).
39. Chappell, A., Hennen, M., Schepanski, K., Dhital, S. & Tong, D. Reducing resolution dependency of dust emission modeling using albedo-based wind friction. *Geophys. Res. Lett.* **51**, e2023GL106540 (2024).
40. Lu, H., Raupach, M. R. & Richards, K. S. Modeling entrainment of sedimentary particles by wind and water: a generalized approach. *J. Geophys. Res. Atmos.* **110**, D24114 (2005).
41. Cui, M., Lu, H., Wiggs, G. F. S., Etyemezian, V., Sweeney, M. R. & Xu, Z. Quantifying the effect of geomorphology on aeolian dust emission potential in northern China. *Earth Surf. Process. Landf.* **44**, 2872–2884 (2019).
42. Sankey, J. B., Caster, J., Kasprak, A. & Fairley, H. C. The influence of drying on the aeolian transport of river-sourced sand. *J. Geophys. Res. Earth Surf.* **127**, e2022JF006816 (2022).
43. Mejia, J. F., Gillies, J. A., Etyemezian, V. & Glick, R. A very-high resolution (20 m) measurement-based dust emissions and dispersion modeling approach for the Oceano Dunes, California. *Atmos. Environ.* **218**, 116977 (2019).
44. Van Pelt, R. S. et al. Dust emission source characterization for visibility hazard assessment on Lordsburg Playa in Southwestern New Mexico, USA. *Geoenviron. Disasters* **7**, 34 (2020).
45. Webb, N. P. et al. Magnitude shifts in aeolian sediment transport associated with degradation and restoration thresholds in drylands. *J. Geophys. Res. Biogeosci.* **130**, e2024JG008581 (2025).
46. Bergametti, G. et al. Dust uplift potential in the central Sahel: an analysis based on 10 years of meteorological measurements at high temporal resolution. *J. Geophys. Res. Atmos.* **122**, 12, 433–12,448 (2017).
47. Zender, C. S., Bian, H. & Newman, D. Mineral Dust Entrainment and Deposition (DEAD) model: description and 1990s dust climatology. *J. Geophys. Res. Atmos.* **108**, 4416 (2003).
48. Webb, N. P., Chappell, A., LeGrand, S. L., Ziegler, N. P. & Edwards, B. L. A note on the use of drag partition in aeolian transport models. *Aeolian Res.* **42**, 100560 (2020).
49. Kandakji, T., Gill, T. E. & Lee, J. A. Drought and land use/land cover impact on dust sources in Southern Great Plains and Chihuahuan Desert of the U.S.: Inferring anthropogenic effect. *Sci. Total Environ.* **755**, 142461 (2021).
50. Nobakht, M., Shahgedanova, M. & White, K. New inventory of dust emission sources in Central Asia and northwestern China derived from MODIS imagery using dust enhancement technique. *J. Geophys. Res. Atmos.* **126**, e2020JD033382 (2021).
51. Warren, A. et al. Dust-raising in the dustiest place on earth. *Geomorphology* **92**, 25–37 (2007).
52. Chappell, A., Warren, A., O'Donoghue, A., Robinson, A., Thomas, A. & Bristow, C. The implications for dust emission modeling of spatial and vertical variations in horizontal dust flux and particle size in the Bodélé Depression, Northern Chad. *J. Geophys. Res. Atmos.* **113**, D00C19 (2008).
53. Kunkelova, T., Crocker, A. J., Wilson, P. A. & Schepanski, K. Dust source activation frequency in the Horn of Africa[J]. *J. Geophys. Res. Atmos.* **129**, e2023JD039694 (2024).

54. Hennen, M. et al. A new framework for evaluating dust emission model development using dichotomous satellite observations of dust emission. *Sci. Total Environ.* **912**, 169237 (2024).
55. Zhang, H., Fan, J., Cao, W., Harris, W., Li, Y., Chi, W. & Wang, S. Response of wind erosion dynamics to climate change and human activity in Inner Mongolia, China during 1990 to 2015. *Sci. Total Environ.* **639**, 1038–1050 (2018).
56. Bergametti, G. et al. Rain, wind, and dust connections in the Sahel. *J. Geophys. Res. Atmos.* **127**, e2021JD035802 (2022).
57. Wang, X. & Zhang, C. Sensitivity of soil dust emissions to driving factor variability in earth's main drylands. *Geoderma* **445**, 116876 (2024).
58. Shao, Y. & Klose, M. A note on the stochastic nature of particle cohesive force and implications to threshold friction velocity for aerodynamic dust entrainment. *Aeolian Res.* **22**, 123–125 (2016).
59. Marshall, J. K. Drag measurements in roughness arrays of varying density and distribution. *Agric. Meteorol.* **8**, 269–292 (1971).
60. Chappell, A. et al. Improving ground cover monitoring for wind erosion assessment using MODIS BRDF parameters. *Remote Sens. Environ.* **204**, 756–768 (2018).
61. Li, X. & Strahler, A. H. Geometric-optical bidirectional reflectance modeling of a conifer forest canopy. *IEEE Trans. Geosci. Remote Sens.* **GE-24**, 906–919 (1986).
62. Wanner, W., Li, X. & Strahler, A. H. On the derivation of kernels for kernel-driven models of bidirectional reflectance. *J. Geophys. Res.* **100**, 21077–21089 (1995).
63. Zhou, Z., Chappell, A., Zhang, C., & Song, H. Satellite retrieved soil surface dynamics reduce the extent and frequency of sediment flux with implications for early warning systems [Data set]. Zenodo. https://doi.org/10.5281/zenodo.18565743 (2026).
64. Chappell, A., & Zhou, Z. Google Earth Engine scripts for the dynamic entrainment areal threshold (dEARTH). Zenodo. https://doi.org/10.5281/zenodo.18599174 (2026).
65. Darmenova, K., Sokolik, I. N., Shao, Y., Marticorena, B. & Bergametti, G. Development of a physically based dust emission module within the Weather Research and Forecasting (WRF) model: assessment of dust emission parameterizations and input parameters for source regions in Central and East Asia. *J. Geophys. Res. Atmos.* **114**, D14201 (2009).

Acknowledgements

The authors are grateful to Google for providing the services of the Google Earth Engine (GEE) and to the global data providers including NASA for MODIS albedo data, ECMWF for ERA5-Land wind and soil moisture data, and ISRIC for SoilGrids particle size data, accessed via the GEE data catalogue. The authors acknowledge financial support from National Natural Science Foundation of China (Grant No. U21A2001) and the State Key Laboratory of Earth Surface Processes and Resource Ecology (2024-ZD-02). The first author acknowledges support from Jiaqi Zhao, Wenping Li, Fanrui Bu, Tongyong Wu and Jianmin Ma for their support in the wind tunnel experiments.

Author contributions

A.C. conceived the research; C.Z. managed the experiments and secured funding for the research. Z.Z., A.C. and C.Z. conducted the research and wrote the initial draft of the paper. All authors reviewed and edited the paper.

Competing interests

The authors declare no competing interests.

Additional information

Supplementary information The online version contains supplementary material available at https://doi.org/10.1038/s43247-026-03368-4.

Correspondence and requests for materials should be addressed to Adrian Chappell or Chunlai Zhang.

Peer review information *Communications Earth & Environment* thanks Eli Argaman and other anonymous, reviewer(s) for their contribution to the peer review of this work. Primary Handling Editors: Mengze Li and Somaparna Ghosh A peer review file is available.